Eur. Phys. J. E **11**, 191–198 (2003)
DOI 10.1140/epje/i2002-10155-4

THE EUROPEAN PHYSICAL JOURNAL E

Crystallization kinetics and crystal morphology in thin poly(ethylene oxide) films

M.V. Massa[1], K. Dalnoki-Veress[1,a], and J.A. Forrest[2]

[1] Department of Physics & Astronomy and the Brockhouse Institute for Materials Research, McMaster University, Hamilton, ON, L8S 4M1, Canada
[2] Department of Physics and Guelph-Waterloo Physics Institute, University of Waterloo, Waterloo, ON, N2L 3G1, Canada

Received 12 December 2002 and Received in final form 12 May 2003 /
Published online: 2 July 2003 –

Abstract. We present a detailed study of the kinetics of crystallization for thin films of poly(ethylene oxide) (PEO). Measurements of the growth rate have been carried out using optical-microscopy techniques on films of monodisperse PEO. Films with thicknesses from 13 nm to ~ 2 μm were crystallized isothermally at temperatures $\sim 20\,^{\circ}$C below the melting point. A remarkable *non-monotonic* slowing-down of the crystal growth is observed for films with thickness less than $\sim$ 400 nm. The changes in the growth rate from bulk-like values is significant and corresponds to a factor of 40 decrease for the thinnest films studied. The morphologies of isothermally crystallized samples are studied using atomic-force microscopy. We find that a morphology, similar to diffusion-controlled growth (dendritic growth and densely branched growth), is observed for films with $h < 150$ nm. In addition, changes in the morphology occur for thicknesses consistent with changes in the growth rate as a function of film thickness.

PACS. 61.41.+e Polymers, elastomers, and plastics – 68.55.-a Thin film structure and morphology – 81.10.-h Methods of crystal growth; physics of crystal growth

Introduction

Semi-crystalline polymers are of tremendous economic importance and their uses range from sophisticated technological applications to disposable consumer products. In addition, many polymeric systems are used in confined geometries: thin-film devices, coatings, lubricants, etc. Questions of general importance relate to the changes that occur when polymeric systems crystallize in a confined geometry. The expectation is that fundamental studies into crystallization in confinement may help us to gain additional understanding of polymer crystallization in general. It is perhaps not surprising that after many decades of work on crystallization in polymer systems there are still many fundamental questions —crystallization in polymers is a complex process requiring the self-organization of large chains into smaller stems which can assemble to form lamellar structures [1]. This process is dependant on kinetic considerations: the mechanisms that can reduce the free energy of the system most rapidly are favoured, resulting in metastable growth structures. Studies of crystallization in confinement can be motivated by the following facts: 1) crystal growth in polymeric systems is kinetically controlled [1], and 2) many studies have shown that dynamics of amorphous polymeric systems are affected by *finite-size* or *chain-confinement* effects [2,3]. For example, at the chain coil length scale, self-diffusion has been shown to be perturbed from "bulk-like" behaviour [4,5], while at the segmental length scale, the glass transition and associated dynamics can also be seen to deviate from that observed in the bulk [2,3]. Various schemes have been used to study polymer crystallization in confinement. The multitude of micro-phases of block-copolymer systems can be used to study confinement in spheres, channels or lamellae, where one of the components confines a crystallizable block [6–10]. Perhaps the most versatile system is confinement into thin films, where the thickness can typically be easily controlled [11–24]. All of these studies have shown that the morphology, crystallinity, or the crystal growth kinetics in confinement are in some way affected.

The literature regarding polymer crystallization in thin films has been growing steadily in recent years. Many of the experiments are measurements of isothermal crystallization, where the crystallization temperature is held at T_c. Here we provide details on some of the thin-film work that is most relevant to the results presented in this manuscript. A series of papers by Frank, Despotopoulou and co-workers studied confinement effects in samples of poly(di-*n*-hexyl silane) [11–13]. They observed reductions

[a] e-mail: dalnoki@mcmaster.ca

in the rate of crystallization and the overall crystallinity with decreasing film thickness. The crystallization rate decreased steadily from the bulk value for thicknesses $h <$ 50 nm. Studies conducted on isotactic polystyrene (it-PS) in Miyaji's group [14,15] showed that the crystal growth rate, G, decreased with decreasing h. A minimum value of G was obtained for the thinnest films with $h = 25$ nm which corresponded to 75% of the bulk value. At a particular value of T_c, the data obtained on it-PS could be described by a simple relation, $G(h) = G(\infty)(1 - d/h)$ with $d = 6$ nm, and d was found to be independent of T_c and M_w, as well as the substrate used. It was suggested that the transport of amorphous material to the growth front is responsible for the anomalous kinetics. The same group also found that the morphology of crystallization was affected in thin films [16,17].

The characterization of crystal morphology in polymer systems is greatly facilitated by atomic-force microscopy (AFM). When applied to polymer systems, which typically exhibit slow growth kinetics, AFM can even be used to provide high-resolution imaging of crystal structures as they evolve in time. The crystallization and melting of PEO lamellae was studied by Pearce and Vancso [18]. These authors showed that the lamellar growth velocities measured using AFM matched the spherulitic growth rates found with optical microscopy (*i.e.* small length scale kinetics was in agreement with much larger length scale kinetics). They also observed a depletion zone of amorphous material in the region immediately in front of the crystal. In a recent study, Li and co-workers examined lamellar growth processes, and observed branched growth as well as the "nucleation" of new lamellae from the partially ordered region at the fold surface of an existing lamella [25]. Hobbs *et al.* found that the growth rates could vary between individual lamellae and also change with time within a single lamella [26]. This work also demonstrated the sensitivity of lamellae to their surrounding environment by showing approaching lamellae redirect their growth to avoid meeting.

In a series of seminal papers by Reiter, Sommer and co-workers, AFM was used to study the crystal morphology in ultrathin PEO samples [19–21]. The films were found to dewet on the substrate leaving behind a thin adsorbed monolayer of PEO. This adsorbed layer, a quasi–two-dimensional system, was found to nucleate crystals only at defects, and most of the crystallization was initiated in the thick dewetted droplets of the PEO. The AFM images show a fractal-like fingering instability which is reminiscent of *diffusion-limited aggregation* (DLA) morphologies [27–29]. A characteristic length scale of the fingers was measured which decreased with T_c, and they also observed a depletion region ahead of the crystal growth front. Reiter, Sommer and co-workers were able to reproduce the growth morphology with computer simulations. Sakai *et al.* observed fingering patterned growth morphologies in crystal terraces which formed within very thin films of poly(ethylene terephthalate) [22]. The growth front was found to exhibit a periodic fingering pattern with a well-defined length scale. In some cases the growth tip would branch into two causing *tip-splittings*. Sakai and co-workers also attributed the behaviour to *diffusion-controlled processes*, and reproduced these growth morphologies in computer simulations, where surface tension and crystal anisotropy were found to play a crucial role. Taguchi and co-workers have observed similar structures in 11 nm films of it-PS, which they also interpreted in terms of diffusion-controlled processes [16]. Their study revealed transitions from *facetted growth* to *dendritic growth* to a *dense branching morphology* (DBM) as T_c is decreased. These researchers suggest that the difference in height between the crystal and a depletion zone of amorphous material establishes a thickness gradient at the crystal-melt interface. It is this gradient which is considered as the source of the unstable growth front [16]. For thicker films the shallow depletion contributes less, and it was observed that these diffusion-controlled morphologies were absent for films with $h > 20$ nm.

We have previously reported a significant slowing-down of the crystal growth rate from bulk-like values for thin PEO films on several substrates [30]. In particular, we observed no change in G as h was decreased from 1000 nm to 200 nm. However, further decreases in h resulted in monotonic reductions in G by as much as a factor of 3 for the thinnest films studied ($h = 40$ nm). The analysis provided suggested that the chain transport was modified from the bulk and was responsible for the reductions in G. In the current paper we report further results of $G(h)$ obtained with optical microscopy for films as thin as 13 nm. The measurements that will be presented below have significantly better resolution compared to our previous work. We find that the $G(h)$ data does not decrease monotonically with decreasing h in contrast with previous measurements [11–15,17,30], rather we see for the first time a *complex dependence* of G on h. It is interesting to note that Hutter and Bechhoefer have studied spherulitic growth in a liquid crystal and observed similar non-monotonic changes in the growth rate as a function of the degree of undercooling [31,32]. In order to characterize the complex behaviour of the growth rate, we use AFM to study the surface topography which reveals a morphology similar to that observed by others [16,17,19–22].

Experiment

High molecular weight ($M_w = 304600$), monodisperse ($M_w/M_n = 1.12$) PEO obtained from Polymer Source (Dorval, Quebec, Canada) was dissolved in acetonitrile. Mass fractions ranging from 0.50 to 3.00% were spincoated with spin speeds ranging from 1500 to 7000 r.p.m. onto Si substrates with the ~ 5 nm native oxide layer present. The Si substrates were cleaned with a jet of argon and then rinsed with acetonitrile immediately prior to spincoating. The film thicknesses studied ranged from 10 to 500 nm, as measured with atomic-force microscopy. In addition, we prepared "bulk-like" films by solvent casting ($h > 1000$ nm).

Crystallization was performed in a commercial hot-stage (Linkam THMS-600) which provided temperature

control to within 0.1 °C. The sample was loaded into the hot stage at room temperature and was surrounded by a thin Al ring with a glass coverslip placed on top which could be lowered and raised externally. With the glass coverslip lifted up and the lid (with viewing port) closed, the sample was flushed with argon for 3 minutes at the isothermal crystallization temperature $T_c = 46\,°C$ and then sealed. The sample was subsequently held at T_c for an additional 7 minutes. This reduces thermal gradients within the stage by equilibrating the bulk of the stage at the temperature at which the measurements are to be performed. We flushed with argon to alleviate concerns associated with a humid environment. The coverslip was then lowered onto the Al ring, thereby enclosing the sample in a very small volume and further reducing any thermal gradients. As will be apparent later, the temperature must be controlled in a very reproducible manner in order to ensure data with minimal error because of a high sensitivity of the crystal growth rate to the temperature. The temperature was subsequently raised ($\sim 20\,°C$/min) to an annealing temperature $T_a = 70\,°C$, which is greater than the ideal melting point of PEO, $T_m = 68\,°C$, for 1 minute. This was found to sufficiently melt the crystallites formed upon spincoating, as will be discussed below. The sample was allowed to cool to $T_c = 46\,°C$ which takes approximately 4 minutes.

The crystal growth front was monitored using optical microscopy with nearly crossed polarisers. Image sequences taken with a CCD camera enabled high-precision measurements of the crystal growth rate G. The growth front was easily resolvable for film thicknesses down to $\sim$ 50 nm. However, for thinner films contrast enhancement of the images was required to distinguish between the crystalline and amorphous regions.

The surface morphology of the crystallized films was characterized using atomic-force microscopy (TM microscopes Explorer, Veeco) where topography images were taken in contact mode at room temperature. Scan sizes between 10 and 50 microns best revealed the crystal structures for all film thicknesses.

Results and discussion

In Figure 1(a) is shown a typical sequence of images for a sample with film thickness $h = 130$ nm. From such images it is straightforward to obtain the change in the crystal radius $R(t) - R_0$, where R_0 is the initial position of the crystal boundary and $R(t)$ the position at time t. Figure 1(b) shows a plot of $R - R_0$ as a function of time, t, from which we obtain the crystal growth rate: $G(h) = \mathrm{d}(R - R_0)/\mathrm{d}t$.

Before performing measurements each sample was annealed in argon at a temperature of 70 °C for 1 minute. The intent of the annealing procedure is to completely melt the crystallized chains, remove any residual solvent and suitably relax the polymer chains from the crystalline morphology (*i.e.* since the surface of a crystallized film is rough which may influence the growth rate, we must relax this surface roughness). Our reasons for annealing at a low temperature (70 °C) for short times are twofold:

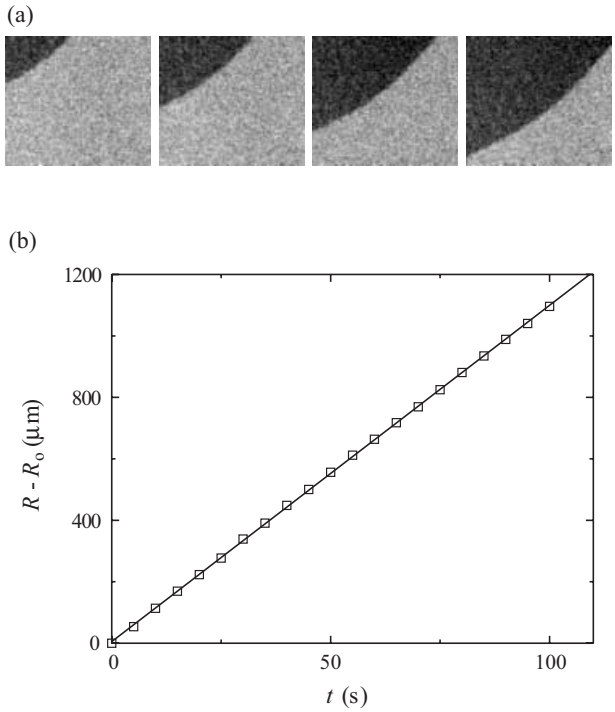

Fig. 1. (a) A typical sequence of images of a crystal growth front taken with optical microscopy with nearly crossed polarisers ($h = 130$ nm). The time interval between images is 10 s, and each image is 750 μm wide. The change in the crystal radius as a function of time for the sample shown in (a) is plotted in (b).

1) The thinnest films studied, $h = 13$ nm, can dewet on the substrate, thereby inducing a topology that does not correspond to a flat and uniform film surface. To facilitate comparison, it is important that the same annealing history can be used for all samples which was possible for the annealing conditions used. 2) It is our intent to perform the same measurements for different M_w values of PEO to probe chain confinement effects. We performed measurements which show that the annealing procedure used ensures no dewetting of the samples for a combination of molecular weight and film thickness as low as $M_w \sim 27000$ and $h = 40$ nm.

In order to verify that the annealing history is sufficient, we performed three tests. First of all, values for the crystal growth rate were conducted over a range of annealing times, t_a for a 130 nm film. We observe that for t_a ranging from 1 to 80 min, there is no deviation in the measured value of G.

Immediately after spincoating, the samples are amorphous and the sample surface is flat compared to the crystallized films. Because these samples are solvent-quenched at room temperature into the amorphous state (*i.e.* supercooled by about 50 °C), they crystallize rapidly. It is these crystallized samples that are subsequently melted and studied. The basis of our second test is that there exists a very short time window after the spincoating where at least parts of the sample remain amorphous and have surface roughness characteristic of amorphous spincoated

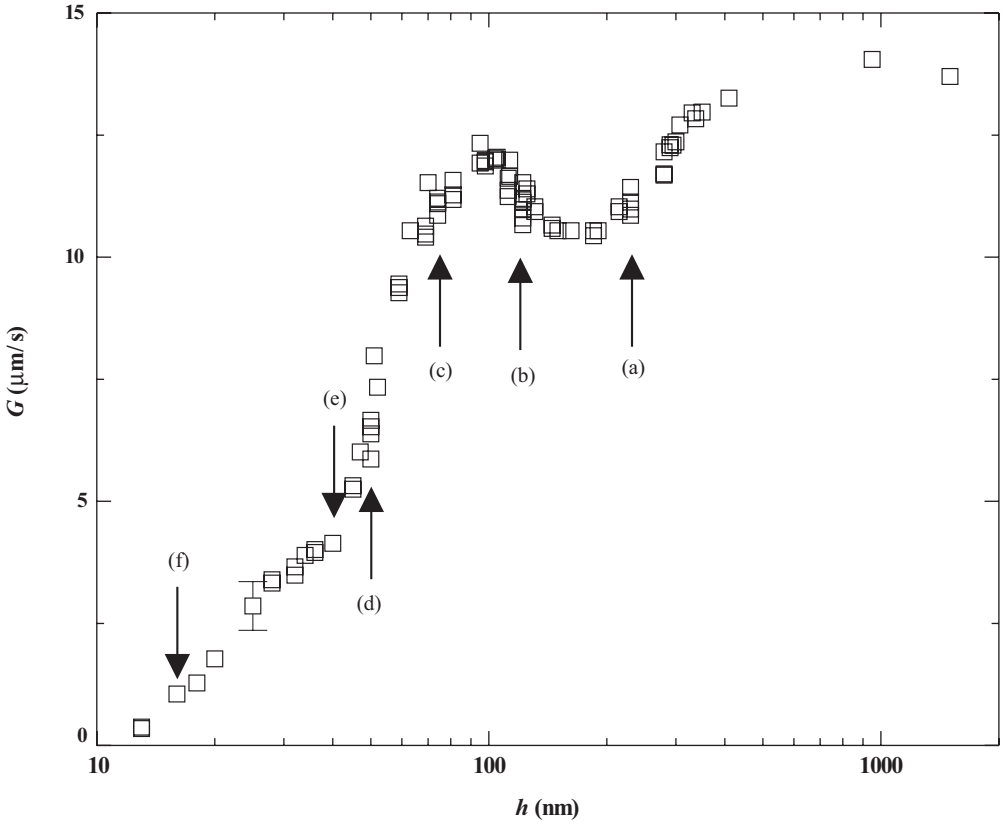

Fig. 2. Crystal growth rate, G, plotted as a function of film thickness, h. The labels indicate the film thicknesses whose images are shown in Figure 3.

films rather than crystallized films. Samples were quickly transferred from spincoater to the hot stage before the entire film was able to crystallize. The crystal growth was inhibited by holding the film at 59 °C (small undercooling), while the standard crystallization procedures were employed (flushing with argon, annealing). The crystal growth rate was then measured within areas of the film that had remained amorphous *throughout the entire process*. The values of G in these measurements showed *no deviation* within experimental uncertainty from those found in samples prepared with our standard methods.

The third test of our annealing procedure was similar to our second approach. Portions of a sample that had never crystallized using the procedure described above were annealed for a long time (10 hours). This was done to ensure that the chains were fully relaxed from the spincoating procedure. Again, no deviation in the growth rate was observed from growth rates measured using our standard annealing procedure. From these three tests we conclude that the samples were adequately annealed for the purposes of measuring growth rates.

The crystal growth rate, G, was measured in over 40 films and in Figure 2 we show G as a function of the film thickness h. It is immediately apparent that the behaviour differs appreciably from previous studies where simple monotonic reductions from bulk values of G were observed [11–15,17,30]. In particular, these results are *qualitatively different* from our own previous measurements of the same system, although they are in agreement within experimental uncertainty [30]. A number of features stand out: as we decrease the film thickness, we first observe deviations from "bulk-like" values of G for $h \sim 400$ nm. At $h \sim 150$ nm G reaches a minimum and starts to increase with decreasing h, resulting in a peak at $h \sim 100$ nm. G decreases monotonically with decreasing h below the peak, however there is a distinct "kink" in the data at a thickness $h \sim 45$ nm. Though it should *only be viewed as an empirical observation*, the region below the kink ($h < 40$ nm) and just above the dip ($h > 150$ nm) both follow a well-defined straight line on the semi-logarithmic plot (*i.e.* $G = G' \ln(h/h_0)$, with $G' = 3.27 \pm 0.05$ μm/s and $h_0 = 12.4 \pm 0.5$ nm). The growth rate data show for the first time that there are multiple transitions in the crystallization kinetics as a result of thin-film confinement that have not been previously reported.

Atomic-force microscopy was employed to obtain insight into the crystallization kinetics by analyzing the surface topography. In Figure 3 we show the topography images taken at different film thicknesses. Labels are provided in Figure 2 which identify the image corresponding to the $G(h)$ data. In order to facilitate comparison of the images, the lateral scale was kept constant where possible (*i.e.* the scan size for Figs. 3(a)-(c) was 50 μm and the scan size for Figs. 3(d)-(f) was 10 μm). Again, we discuss these results with decreasing film thickness, starting with the image corresponding to the thickest film. In Figure 3(a)

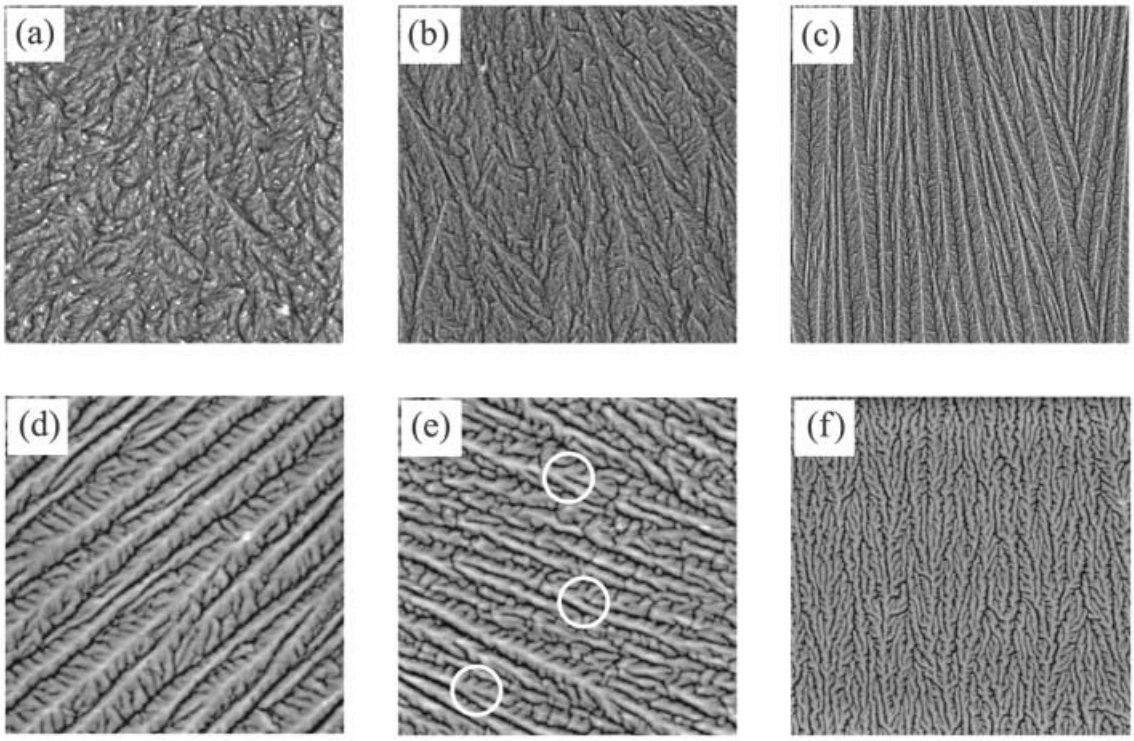

Fig. 3. AFM images showing the surface topography for selected films. The images are representative of the morphologies observed for different values of h: (a) $h = 230$ nm, (b) $h = 120$ nm, (c) $h = 75$ nm, (d) $h = 47$ nm, (e) $h = 43$ nm, and (f) $h = 17$ nm. Tip-splittings shown in (e) are indicated by the circles. Images (a)-(c) are 50×50 μm scans, and images (d)-(f) are 10×10 μm scans. The approximate height scale of the images is 80, 55, 50, 30, 30, and 20 nm, respectively. Labels are provided in the plot of $G(h)$ (Fig. 2) to facilitate comparison.

($h = 230$ nm), the surface exhibits a nearly isotropic surface morphology which is characteristic of samples that are isothermally crystallized in very thick films with $h \sim 2$ μm (there is some anisotropy in the morphology due to the growth direction of the crystal front). There is little difference in the morphology from that of "bulk-like" films even though we are at a film thickness where there is a definite, albeit small, deviation from bulk values of G. For these thick films we also observe lamellae that appear in all orientations including "edge-on" where the lamellae are perpendicular to the substrate. In contrast to the isotropic morphology of Figure 3(a), the surface morphology in Figure 3(b) ($h = 120$ nm) displays prominent ridges or *backbones* which appear throughout the surface. At this stage, these backbone structures appear infrequently, and are oriented roughly radially out from the nucleus of the crystal, although the angular distribution is broad. Another morphological change is that, as the thickness is decreased below the bulk, the number of "edge-on" lamellae diminishes, and are not observed below $h \sim 150$ nm. This length scale coincides with the onset of the backbone structures. It is worth noting that both films (Figs. 3(a),(b)) exhibit the same crystal growth rate because the two thicknesses are located on opposite sides of the dip $G(h)$ (see Fig. 2). The formation of these backbones as G increases with decreasing h represents the onset of a new growth mechanism in the film thickness ranges from 100 to 150 nm, which has structural characteristics that are similar to those found in diffusion-controlled growth (DCG). This is similar to the morphologies observed in the work by Reiter *et al.* for ultrathin PEO films [19–21].

A comparison of Figures 3(b) and (c) ($h = 75$ nm) shows the progression of the backbone structures: with decreasing film thickness, there is a greater angular coherence of the backbones and they are more densely packed. It should be noted that in Figures 3(a)-(c) the crystal growth rates are roughly equal. Films with $h < 100$ nm are associated with a high density of backbones. To the right of the peak ($100\,\text{nm} < h < 150\,\text{nm}$) the density of backbones is low and this regime represents the onset of a different growth mechanism from the bulk, which is analogous to DCG. We speculate that as the thickness decreases below 100 nm, the tightly packed backbones impinge upon their neighbours which may be a contributing factor in the observed reduction in G. As we decrease the film thickness further (Figs. 3(d)-(f), note the change in scan size) it is clear that the morphology is reminiscent of the dendritic DCG structures that are commonly found in viscous-fluid displacement in Hele-Shaw cells [33], electrodeposition experiments [34], and also the polymer crystallization studied by others [16,17,19–22]. In this morphology, the backbone marks the primary growth of the dendrite, from which the secondary fingers branch and grow, until the neighbouring dendrite is reached. The spacing of the secondary fingers, and the distance between backbones both appear to have some well-defined

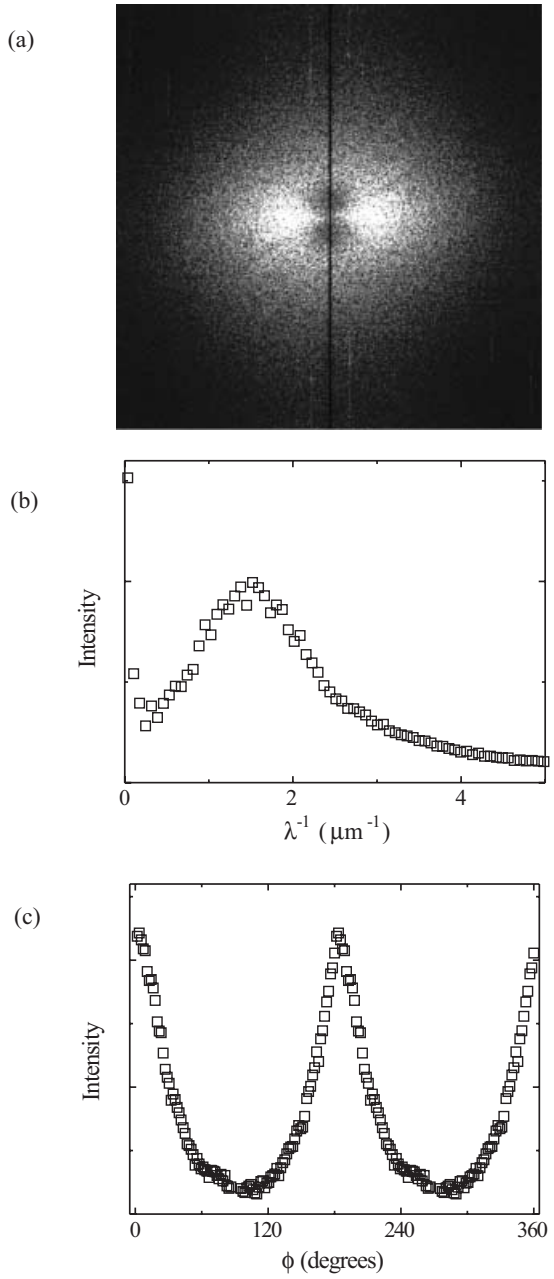

Fig. 4. A typical example of the Fourier analysis showing a two-dimensional FFT of the image shown in Figure 3(f) for a film with $h = 17$ nm (a), with the corresponding radial (b), and angular (c) distributions.

average value. The selection of a particular length scale is typical for DCG and will be quantified below.

The "kink" in the $G(h)$ data at $h \sim 45$ nm (Fig. 2) marks a change in the growth mechanism. In order to elucidate this change, we show Figures 3(d) and (e) which differ in film thickness by *only* 4 nm and are in the "kink" region ($h = 47$ nm and $h = 43$ nm, respectively). Besides the decreasing length scale in the topology with decreasing film thickness, the morphology becomes qualitatively different at the "kink". As we decrease the film thickness, the onset of this transition is characterized by a decrease in separation between backbones as well as a decrease in the width of the backbones to a size that is comparable to the width of the side branches. At this stage there is less distinction between the backbone and the side branches and an increased number of tip-splittings is observed. This tip-splitting is only prevalent for films with thickness below the "kink" ($h < 40$ nm), and the DCG morphology persists, but the morphology is qualitatively different. Figure 3(f) ($h = 17$ nm) shows a lamellar orientation that is "flat-on" (*i.e.* parallel to the surface), which is typical of the thinnest films. For this film thickness the primary and secondary growth fingers no longer differ in size, and tip-splittings occur with great frequency resulting in less angular coherence of the growth structures (*i.e.* greater anisotropy). These growth features are characteristic of the so-called *compact-seaweed* (CS) or *dense-branching* morphology (DBM) commonly observed in systems that exhibit DCG [35].

It is apparent that many of the features observed in the $G(h)$ data coincide with changes in the growth morphology. A Fourier analysis was used to quantify the changes in the morphology as a function of the film thickness. A two-dimensional Fast Fourier Transform (FFT) was made of the AFM images that displayed diffusion-controlled morphologies (*i.e.* for $h < 150$ nm —thicker films exhibit bulk-like morphologies). A typical example of the analysis is shown in Figure 4 for the film with $h = 17$ nm (Fig. 3(f)). The analysis was performed as follows. The FFT was obtained from the real-space images (Fig. 4(a)) and was used to plot the radial distribution (Fig. 4(b)) as well as the angular distribution (Fig. 4(c)) of the intensity. In order to measure the dominant length scale, λ, of the backbone structures, a Gaussian signal peak plus an inverse-frequency background is fit to the radial distribution data. This fitting procedure is *not* based on a physical model of the distribution, rather an approach was required that would result in a consistent method to obtain the peak position. The plot of $\lambda(h)$ is shown in Figure 5(b) and in order to facilitate comparison we also reproduce $G(h)$ with the same horizontal axis (Fig. 5(a)). There is some scatter for thicker films ($100\,\text{nm} < h < 150\,\text{nm}$) which can be attributed to the lack of coherence of the dendritic backbones as they first appear. The logarithmic plot appears linear over the entire range of thicknesses; however, with the uncertainties given, we do not discount the possibility of a more complicated relationship between λ and h.

A measure of the anisotropy of the growth was obtained from the angular distribution of which a typical example is shown in Figure 4(c). The data is well described by a Lorentzian peak which is used to obtain the full width at half-maximum ($\Delta\theta$). Again, the fit is empirical and is only used to provide a reproducible method for quantifying the anisotropy. If $\Delta\theta$ is large, then this indicates little angular coherence between the backbones and a more isotropic morphology. Conversely, a smaller value of $\Delta\theta$ implies that the backbones are arranged parallel to each other resulting in an anisotropic morphology. The results of this anisotropy analysis are shown in Figure 5(c).

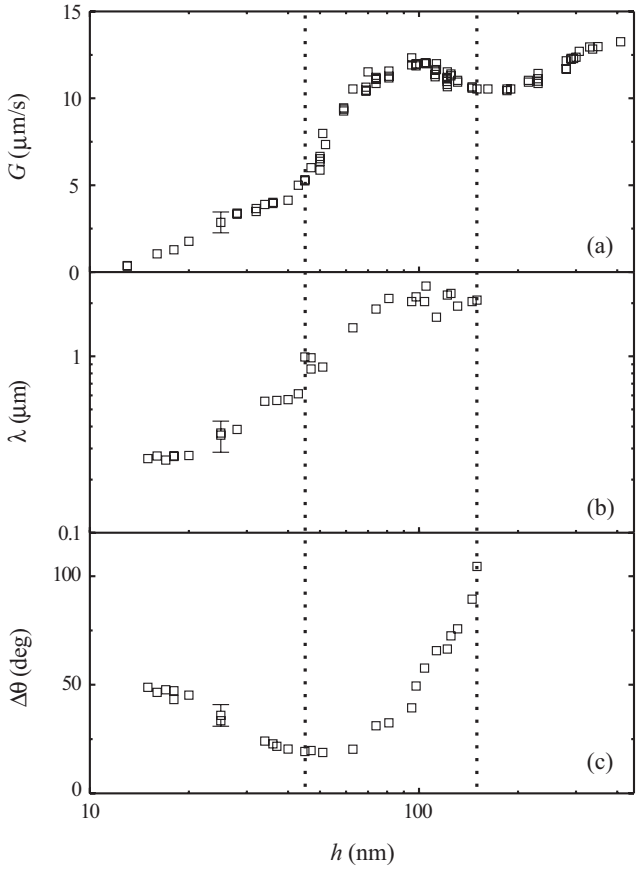

Fig. 5. Plot of the crystal growth rate and the measured morphology parameters as a function of the film thickness. The crystal growth rate $G(h)$ (a), dominant wavelength of the growth morphology $\lambda(h)$ (b), and the full width at half-maximum of the angular distribution $\Delta\theta(h)$ (c) are all plotted with the same horizontal axis. The dotted lines identify the transitions from bulk to dendritic growth at $h \approx 150$ nm and from dendritic to dense-branching growth at $h \approx 45$ nm.

With the procedure discussed we are able to quantify the features observed in the AFM images (Fig. 3). As the film thickness is decreased from $\sim$ 150 nm to $\sim$ 45 nm, backbones appear and become more prevalent resulting in a closer spacing and a greater anisotropy. These features are observed in the plots of $\lambda(h)$ and $\Delta\theta(h)$. With further decreases in the film thickness, the wavelength, λ, continues to decrease; however at the "kink" ($h = 45$ nm) the value of $\Delta\theta$ starts to increase again. This subsequent broadening of the angular distribution in the thinnest films agrees with the observed increase in the number of tip-splittings, which cause the crystal fingers to splay outwards and loose angular coherence.

Both the surface morphology and the crystal growth rate data indicate a significant change from the growth mechanism in bulk systems as the degree of confinement is increased. The appearance of the dendritic and dense branching structures strongly suggest that the decrease in film thickness results in growth kinetics that are controlled by the diffusion of amorphous material to the growth front. Such diffusion-controlled processes are commonly found in two-dimensional electrodeposition, viscous fluid flow, and melt-solidification experiments [33,34]. In these systems, the growth of a smooth interface becomes unstable under a small driving force. The selection of a specific morphology is sensitive to intrinsic properties such as the surface tension. Thermal gradients, created by the removal of latent heat, are known to cause instabilities at the crystal interface. However, the thermal diffusion lengths of polymers are typically on the order of centimeters to meters [15], making heat transport a minor factor in the formation of these growth patterns.

In the study of it-PS [16], it was suggested that the driving force was the result of the difference in height between the lamella and the much thinner region of amorphous material ahead of the growth front. A depletion zone, observed in several studies of polymer crystal growth, arises from the difference in density at the solid-melt interface [15–19]. However, there are two significant differences between the behaviour observed in it-PS films and the results presented in this article: 1) The morphologies found in 11 nm it-PS films were not present in films thicker than 20 nm. This was attributed to a strong dependence of the driving force on the relative thickness of the depletion region to the overall film thickness. In contrast to this, diffusion-controlled morphologies are observed in PEO films as thick as $\sim$ 150 nm. 2) The transitions from *facetted growth* to *dendritic growth* to *densely branched growth* follow from a decrease in the crystallization temperature, and are observed at a fixed film thickness. In our studies the progression of morphologies in PEO films from *bulk-like growth* to *dendritic growth* to *densely branched growth* corresponds to a reduction in film thickness at a constant crystallization temperature. Similar growth morphologies were also observed by Reiter, Sommer and co-workers [19–21]. In their work, the crystallization of adsorbed monolayers of PEO was compared to simulations with a basis in diffusion-limited aggregation [27]. In work done on a liquid-crystalline system non-monotonic changes in the growth rate of spherulites were observed with decreasing temperature [31,32]. While these studies were on a very different system, and the parameter changed was the temperature rather than film thickness, the similarities in the growth rate dependence may be more than an intriguing coincidence.

There are critical thicknesses at which the crystal growth rate has transitions: we measure deviations from "bulk-like" values of G at $h \sim 400$ nm, a local minimum in G at $h \sim 150$ nm, a peak in G at $h \sim 100$ nm, and finally a "kink" in the growth rate at $h \sim 45$ nm. At present, we do not have a full understanding of the complex growth mechanisms which result in the observed morphologies and dynamics. The inherent length scales of the system are the lamellar thickness $\sim$ 10 nm and the end-to-end distance of the PEO used $R_{ee} \sim 50$ nm [36]. While it is possible that the "kink" in growth rate at $h \sim 45$ nm may be associated with R_{ee}, all the other length scales are much larger. Perhaps most relevant are measurements which indicate that chain diffusion in confinement can be significantly affected at length scales that are 5–10 times as large as R_{ee} [4,5].

The reductions in the diffusion may be, at least in part, a reason for the reductions in the crystal growth rate for thin films. Our discussion in terms of the well-established diffusion-controlled behaviour is strongly suggested by the morphologies, but it is not clear how the diffusion may be affected in the confined geometry. While we cannot provide a full explanation for the cause of the slowing-down of the crystallization, we can conclude that, regardless of the mechanism, the final morphology displays many features typical of those observed in diffusion-controlled processes.

Conclusions

In this paper we described the results of an extensive study of the isothermal crystallization growth rate, G, in thin films of PEO. Optical microscopy was used to measure the growth rate for films ranging in thickness from 13 nm to 2 μm. The larger errors associated with previous results obstructed a rather complex non-monotonic dependence of G on the films thickness which is only apparent in these new data. The reduction in the growth rate from bulk-like values is significant, corresponding to a factor of 40 for the thinnest films. These measurements of the growth rate were complemented by AFM measurements of the surface topography. Surprisingly, transitions in the growth rate dependence on the film thickness could be linked directly to changes in the morphology. For films with $h < 150$ nm, we observed the emergence of a process similar to diffusion-controlled growth as observed previously in much thinner films ($h \sim 10$ nm) [16,17,19–22].

Financial support from NSERC of Canada, the Canadian Foundation for Innovation and the Ontario Innovation Trust is gratefully acknowledged.

References

1. G. Strobl, *The Physics of Polymers: Concepts for Understanding Their Structures and Behaviour*, second edition (Springer-Verlag, Berlin, 1997).
2. J.A. Forrest, R.A.L. Jones, in *Polymer Surfaces Interfaces and Thin Films*, edited by A. Karim, S. Kumar (World Scientific, Singapore, 2000) and references therein.
3. J.A. Forrest, K. Dalnoki-Veress, Adv. Colloid Interface Sci. **94**, 167 (2001) and references therein.
4. B. Frank, A.P. Gast, T.P. Russell, H.R. Brown, C. Hawker, Macromolecules **29**, 6531 (1996).
5. X. Zheng, M.H. Rafailovich, J. Sokolov, Y. Strzhemechny, S.A. Schwarz, B.B. Sauer, M. Rubinstein, Phys. Rev. Lett. **79**, 241 (1997).
6. B. Lotz, A.J. Kovacs, Kolloid Z. Z. Polym. **209**, 97 (1966).
7. L. Zhu, B.H. Calhoun, Q. Ge, R.P. Quirk, S.Z.D. Cheng, E.L. Thomas, B.S. Hsiao, F. Yeh, L.Z. Liu, B. Lotz, Macromolecules **34**, 1244 (2001).
8. Y.-L. Loo, R.A. Register, A.J. Ryan, Phys. Rev. Lett. **84**, 4120 (2000).
9. S. Hong, W.J. MacKnight, T.P. Russell, S.P. Gido, Macromolecules **34**, 2876 (2001).
10. G. Reiter, G. Castelein, J.-U. Sommer, A. Röttele, T. Thurn-Albrecht, Phys. Rev. Lett. **87**, 226101 (2001).
11. C.W. Frank, V. Rao, M.M. Despotopoulou, R.F.W. Pease, W.D. Hinsberg, R.D. Miller, J.F. Rabolt, Science **273**, 912 (1996).
12. M.M. Despotopoulou, C.W. Frank, R.D. Miller, J.F. Rabolt, Macromolecules **29**, 5797 (1996).
13. M.M. Despotopoulou, R.D. Miller, J.F. Rabolt, C.W. Frank, J. Polym. Sci. Polym. Phys. Ed. **34**, 2335 (1996).
14. S. Sawamura, H. Miyaji, K. Izumi, S.J. Sutton, Y. Miyamoto, J. Phys. Soc. Jpn. **67**, 3338 (1998).
15. K. Izumi, G. Ping, M. Hashimoto, A. Toda, H. Miyaji, Y. Miyamoto, Y. Nakagawa, in *Advances in the Understanding of Crystal Growth Mechanisms*, edited by T. Nishinaga, K. Nishioka, J. Harada, A. Sasaki, H. Takei (Elsevier Science, Amsterdam, 1997) p. 337.
16. K. Taguchi, H. Miyaji, K. Izumi, A. Hoshino, Y. Miyamoto, R. Kokawa, Polymer **42**, 7443 (2001).
17. K. Taguchi, H. Miyaji, K. Izumi, A. Hoshino, Y. Miyamoto, R. Kokawa, J. Macromol. Sci. Part B Physics **41**, 1033 (2002).
18. R. Pearce, G.J. Vancso, Macromolecules **30**, 5843 (1997).
19. G. Reiter, J.-U. Sommer, Phys. Rev. Lett. **80**, 3771 (1998).
20. G. Reiter, J.-U. Sommer, J. Chem. Phys. **112**, 4376 (2000).
21. J.-U. Sommer, G. Reiter, J. Chem. Phys. **112**, 4384 (2000).
22. Y. Sakai, M. Imai, K. Kaji, M. Tsuji, J. Cryst. Growth **203**, 244 (1999).
23. J. Kressler, C. Wang, H.W. Kammer, Langmuir **13**, 4407 (1997).
24. V.H. Mareau, R.E. Prud'homme, Macromolecules **35**, 5338 (2002).
25. L. Li, C.-M. Chan, K.L. Yeung, J.-X. Li, K.-M. Ng, Y. Lei, Macromolecules **34**, 316 (2001).
26. J.K. Hobbs, A.D. L. Humphris, M.J. Miles, Macromolecules **34**, 5508 (2001).
27. T.A. Witten jr., L.M. Sander, Phys. Rev. Lett. **47**, 1400 (1981).
28. M. Uhawa, Y. Saito, Phys. Rev. A **40**, 4716 (1989).
29. Y. Saito, *Statistical Physics of Crystal Growth* (World Scientific, 1995).
30. K. Dalnoki-Veress, J.A. Forrest, M.V. Massa, A. Pratt, A. Williams, J. Polym. Sci. Polym. Phys. Ed. **39**, 2615 (2001).
31. J.L. Hutter, J. Bechhoefer, Phys. Rev. E **59**, 4342 (1999).
32. J.L. Hutter, J. Bechhoefer, J. Cryst. Growth **217**, 332 (2000).
33. E. Ben-Jacob, G. Deutscher, P. Garik, N.D. Goldenfeld, Y. Lareah, Phys. Rev. Lett. **57**, 1903 (1986).
34. Y. Sawada, A. Dougherty, J.P. Gollub, Phys. Rev. Lett. **56**, 1260 (1986).
35. E. Brener, H. Müller-Krumbhaar, D. Temkin, Europhys. Lett. **17**, 535 (1992).
36. L.J. Fetters, D.J. Lohse, R.H. Colby, in *Physical Properties of Polymers Handbook*, edited by J.E. Mark (American Institute of Physics, Woodbury, N.Y., 1996) Chapt. 24.